Compatibility and microstructure evolution of Al-Cr-Fe-Ni high entropy model alloys exposed to oxygen-containing molten lead

Hao Shi[a,*], Adrian Jianu[a,*], Renate Fetzer[a], Dorothée Vinga Szabó[b,c], Sabine Schlabach[b,c], Alfons Weisenburger[a], Chongchong Tang[b], Annette Heinzel[a], Fabian Lang[a], Georg Müller[a]

[a] *Institute for Pulsed Power and Microwave Technology (IHM), Karlsruhe Institute of Technology (KIT), Hermann-von-Helmholtz-Platz 1, 76344 Eggenstein-Leopoldshafen, Germany*
[b] *Institute for Applied Materials (IAM), Karlsruhe Institute of Technology (KIT), Hermann- von-Helmholtz-Platz 1, 76344 Eggenstein-Leopoldshafen, Germany*
[c] *Karlsruhe Nano Micro Facility (KNMF), Karlsruhe Institute of Technology (KIT), Hermann- von-Helmholtz-Platz 1, 76344 Eggenstein-Leopoldshafen, Germany*

*Corresponding author. E-mail address: hao.shi@kit.edu (H. Shi); adrian.jianu@kit.edu (A. Jianu).

Keywords: AlCrFeNi; High entropy alloy (HEA); Corrosion; Microstructure; Molten lead.

Abstract

Five Al-Cr-Fe-Ni based high entropy model alloys, mainly a mixture of FCC and BCC or single FCC phase, have been designed and prepared. The corrosion tests of as-cast alloys in oxygen-containing molten Pb show their promising corrosion resistances at 600 °C, which is due to the formation of protective $(Fe,Cr)_3O_4/Al_2O_3$ or Cr_2O_3/Al_2O_3 bi-layer. After 2000 h exposure, all alloys are able to maintain the phase compositions obtained from as-cast alloys. However, additional minor phases like σ-phase or precipitation of B2-NiAl either at grain boundaries or adjacent to inter-dendrites are observed.

1. Introduction

Environmentally friendly energy production/conversion technologies are proposed as one of the main future energy solutions, for example, concentrated solar power (CSP) systems, Gen IV fast-neutron reactors, fusion reactors, accelerator-driven systems (ADS), methane cracking and liquid metal batteries (LMB) [1-6]. However, these systems often involve extreme working conditions like high temperature (≥ 450 °C), mechanical loads, and high irradiation doses (in nuclear application) [6-10]. Therefore, heat transfer media with excellent thermo-physical properties, like heavy liquid metals (HLM, e.g. Pb or PbBi eutectic), are proposed to replace the traditional transfer media like air or water [5, 11-14]. However, commercial structural steels (e.g. ferritic-martensitic (F/M) steels, austenitic steels) have shown compatibility issues, especially corrosion sensitivity, when in contact with HLMs [13, 15-16]. The corrosion of steels in HLMs can be in terms of direct dissolution attack (solubility in Pb: Ni>Cr>Fe) or-/and- inter-granular attack with preferential leaching of one or more alloying elements [12, 17-18]. In addition, F/M steels are susceptible to liquid metal embrittlement (LME) in the temperature range of 300 to 425 °C under loading conditions [19].

Controlling the dissolved oxygen concentration in HLMs is one of the most efficient corrosion mitigation strategies in heavy liquid metal environment [20-21]. By introducing a certain amount of oxygen, which is lower than the dissociation oxygen partial pressure of PbO/Bi_2O_3, but higher than that of passive oxide layer formers like $(Fe,Cr)_3O_4$ or-/and- Cr_2O_3, in-situ growth of an oxide based corrosion

inhibitor layer on steel surface is possible. Moreover, recent pioneer research work indicate that austenitic alloys/steels with a low amount of Al addition, called alumina-forming austenitic (AFA) alloys, are able to form a slow growing alumina-rich oxide layer when exposed to liquid Pb [11, 22-24]. However, this type material, with the composition range Fe-(20-29)Ni-(15.2-16.5)Cr-(2.3-4.3)Al (wt.%), actually defines the minimum value of Al, Cr, and Ni, either required for passive oxide layer formation or stabilization of austenitic phase. The concentrations above this given range were never investigated, namely increasing the amount of Al and Cr to create alloys with multi-principle elements.

During the last two decades, a new type of alloys, called high entropy alloys (HEAs) or complex concentrated alloys (CCAs), have been created with unique and even intriguing compositions, microstructures and engineering properties [25-29]. To break the concept of single or double principal elements for conventional steels, multi-principle elements (concentration of each component: 5 to 35 at.%) are introduced in HEAs, which consist of either solid solution (SS) or SS plus inter-metallic compounds (IM) [25, 30]. At the same time, other types of microstructure like amorphous phase (AM) or mixtures of SS, IM or-/and- AM can co-exist in multi-principle elements combinations, depending on the chemical compositions and preparation conditions [27]. To solve this issue, some empirical parameters have been defined to guide the HEA design, including thermodynamic considerations like Gibbs free energy of mixing (ΔG_{mix}), the enthalpy of mixing (ΔH_{mix}), and the entropy of mixing (ΔS_{mix}), as well as the geometrical parameter of atomic size difference (δr) [25, 31-34]. Specifically, the values of ΔH_{mix} and δr are limited to -15 kJ/mol < ΔH_{mix} < 5 kJ/mol and 1% < δr < 6.6% in order to promote the formation of SS or SS plus IM [32]. Another parameter Ω ($\Omega = (\Sigma c_i T_{m,i}) \Delta S_{mix} / |\Delta H_{mix}|$) considers the contribution not only from entropy of mixing (ΔS_{mix}) but also from enthalpy of mixing (ΔH_{mix}) [33]. This parameter can be used together with δr to help separating SS from SS+IM in some cases. The value of Ω should be larger than 1.1 [33]. With the consideration of this criterion, the searching range for HEAs is expanded to the alloys with three or four principle elements. Moreover, Guo et al. [34] discussed the valence electron concentration (*VEC*) of as cast HEAs and indicated its applicability on predicting the formation of BCC or FCC solid solution within the 3d transition metal family. For instance, BCC phase is stabilized with *VEC* less than 6.0 while FCC phase is dominant when *VEC* is larger than 7.8 [34-35]. In case of *VEC* between 6.0 and 7.8, additional inter-metallic compounds tend to form in addition to the FCC or FCC plus BCC solid solutions.

Among the variety of HEAs, Al-Co-Cr-Fe-Ni system/sub-system has shown excellent properties, especially corrosion/oxidation resistance at elevated temperatures [36-38]. However, considering the expensive price of cobalt (Co) and its irradiation sensitivity in nuclear reactor [39], a type of Co-free Al-Cr-Fe-Ni HEA model alloys is proposed targeting for high temperature and aggressive environment applications. Two basic requirements are considered for the novel HEA model alloy design. One is the ability to promote the formation of alumina-rich protective scale, which acts as a corrosion barrier when exposing it to aggressive environments. Another one is the ability to form and maintain the FCC dominant or mixture of FCC and BCC solid solutions in bulk alloys during exposure.

2. Material and methods

2.1 Alloy preparation

The as cast alloys are prepared by arc melting the mixture of high purity elements (purity > 99.99%) with a non-consumable tungsten electrode in argon atmosphere. The ingots have been flipped over and re-melted at least five times in a water chilled copper mold to promote composition homogenization. The facility used in this study is a mini arc melting system (MAM-1, Serial-No.2426220) with the maximum temperature of 4000 °C. The cooling rate of water cooled arc melting is around 100 K/s between 2300 K and 1300 K [40-41].

2.2 Corrosion test

The corrosion experiments have been performed in a stagnant molten Pb corrosion facility, called COSTA (**CO**rrosion test stand for **ST**agnant liquid **A**lloys at Karlsruhe Institute of Technology (KIT)) [12]. Test samples were exposed to molten Pb at 600 °C for 2000 h. The concentration of oxygen dissolved in molten Pb is adjusted to 10^{-6} wt.%, which is reported to promote the formation of alumina-rich oxide scale [23]. More detailed information related to oxygen control has been described in the references [12, 21-22].

The solid Pb is melted and filled in alumina crucibles, subsequently placed on a Ni tray in order to be easily inserted into a quartz tube type furnace. Before the corrosion test, molten Pb is exposed to reducing oxygen condition for 3 days, followed by 7 days at the target exposure conditions. Samples for the corrosion test are cut in discs with a diameter of 10 mm and thickness of 1.2 mm. A hole with a diameter of 1.5 mm is drilled on each sample near the edge. All specimens are grinded to 1200 grit surface finish, cleaned with acetone and ethanol in an ultrasonic bath and dried. Then each sample is hanged using a Mo-wire and fastened to the alumina holder in order to prevent floating during corrosion test.

In order to maintain the oxygen condition in the furnace during experiment, a dedicated glovebox conditioned to a similar oxygen partial pressure is used for sample loading. After connecting the glove-box to the quartz-tube, the Ni-tray with all molten Pb-containing crucibles is transferred into the glovebox. All the specimens are placed in the crucibles and are fully immersed in the molten Pb. During the fast loading process (~3 min), the temperature of liquid Pb drops to 450-500 °C. After the Ni-tray is put back into the quartz-tube, it will take around 10 min to recover to the original temperature. The oxygen concentration in molten Pb will reach the set value within 2 h. During the experimental stage, the oxygen condition is monitored and kept constant.

After the corrosion test, samples were extracted from molten Pb using the same conditioned glovebox as for the loading process. The visual check shows that most of the samples surfaces are shining and only a few areas remained covered by residual, sticking Pb. There, the remaining adherent Pb was cleaned by immersing the samples into a mixed solution of acetic acid, hydrogen peroxide and ethanol (1:1:1) [42].

2.3 Characterization

Microstructures of as cast alloys have been characterized by Scanning Electron Microscopy (SEM, model: Hitachi S-4800 with cold field emission electron source or Philips XL 40 SEM with LaB_6 cathode), equipped with electron dispersive X-ray spectroscopy (EDS). The applied high voltage of the electron beam varies from 10 to 20 kV and a working distance of 10 mm was used.

Besides a careful check of the entire surfaces of exposed samples, the oxide scale structure was further characterized through cross section analysis. The samples were embedded in resin, grinded by sand papers in different levels, e.g. 1200 #, 2400 #, and then polished with diamond paste (1 µm diameter diamond particles). In order to protect the possible oxide scale from grinding damage, a Nickel layer with a thickness of around 25-30 µm has been deposited on the sample surface by the electroplating process previously. To maintain electron conductivity for SEM investigation, a thin gold layer was sputtered on the samples surface and has been included in data evaluation

The phase compositions of as cast and exposed samples were analyzed by X-ray diffraction (XRD, Seifert PAD II) with Cu Kα1 radiation (λ=0.15406 nm, 40 kV and 30 mA) in Bragg–Brentano geometry (θ-2θ) with a step size of 0.02° and a scan speed at 0.1 °/min.

In addition, some exposed alloys were selected to be characterized by Transmission Electron Microscopy (TEM). The TEM samples were prepared by a dual beam Focused Ion Beam (FIB-SEM) system. Lamellae were cut perpendicular to the surface oxide scale down to a depth of 10 µm. Prior to the cutting, a Pt layer was deposited on the target region to protect the surface from Ga-ion impact. The instrument used in this study is FEI Strata 400S equipped with Omniprobe™ 200 micromanipulator. The TEM investigations were done using a FEI Tecnai G^2 F20 ST, operated at 200 keV, equipped with a field emission gun, with an Orius SC600 CCD Camera (Ametek, Pleasantron, California, USA), a S-UTW EDS Si(Li) Detector (EDAX, Mahwah, New Jersey, USA) for elemental analysis, and a HAADF-detector for STEM-mode.

3. Results

3.1 Alloy design

The Al-Cr-Fe-Ni system is considered for the HEA model alloy design. In addition to satisfying the composition definition of HEAs (concentration of each element: 5 to 35 at.%), empirical parameters including ΔH_{mix}, δr, Ω and *VEC* have been employed to tailor the chemical compositions of candidate alloys. Table 1 shows the required values of these parameters according to literatures [26, 31-33], in order to search for the HEA model alloys either with single FCC solid solution or a mixture of solid solutions (FCC+BCC) plus IM phases.

Table 1
Required values of ΔH_{mix}, δr, Ω and *VEC* for HEA design.

Microstructure	ΔH_{mix} (KJ/mol)	δr (%)	Ω	*VEC*

FCC solid solution	$-15<\Delta H_{mix}<5$	$1<\delta r<6.6$	>1.1	>7.8
FCC+IM	$-15<\Delta H_{mix}<5$	$1<\delta r<6.6$	>1.1	7.5 < VEC < 7.8
FCC+BCC+IM	$-15<\Delta H_{mix}<5$	$1<\delta r<6.6$	>1.1	6 < VEC < 7.5

The values of ΔH_{mix}, δr, Ω and *VEC* have been calculated by varying the chemical concentrations of alloying elements to select the potential HEA model alloys. Table 2 shows the nominal compositions of candidate alloys (at.%), mole formula as well as the calculated values of ΔH_{mix}, δr, Ω and *VEC*. Comparing the calculated values with the design rules described above, one sample (HEA-1) is predicted to form FCC, BCC and IM, two alloys (HEA-2, HEA-3) tend to form FCC with IM, and another two compositions (HEA-4, HEA-5) will form single FCC solid solution, see Table 2.

Table 2
Nominal compositions of HEA model alloys (at.%), mole formula and calculated values of ΔH_{mix}, δr, Ω and *VEC*.

Code	Nominal composition (at.%)	Mole formula	ΔH_{mix}	δr	Ω	*VEC*	Predicted Phase
HEA-1	$Al_{9.8}Cr_{30.3}Fe_{33.0}Ni_{26.9}$	$Al_{0.30}Cr_{0.92}FeNi_{0.82}$	-8.32	4.39	2.37	7.44	FCC+BCC+IM
HEA-2	$Al_{11.7}Cr_{22.4}Fe_{33.3}Ni_{32.6}$	$Al_{0.36}Cr_{0.67}FeNi_{0.98}$	-9.33	4.74	2.07	7.62	FCC+IM
HEA-3	$Al_{9.8}Cr_{22.5}Fe_{33.2}Ni_{34.5}$	$Al_{0.30}Cr_{0.68}FeNi_{1.04}$	-8.68	4.40	2.21	7.75	FCC+IM
HEA-4	$Al_{6.0}Cr_{25.0}Fe_{34.0}Ni_{35.0}$	$Al_{0.18}Cr_{0.73}FeNi_{1.03}$	-7.09	3.54	2.67	7.90	FCC
HEA-5	$Al_{8.0}Cr_{23.2}Fe_{34.0}Ni_{34.8}$	$Al_{0.23}Cr_{0.68}FeNi_{1.02}$	-7.91	4.03	2.41	7.83	FCC

Fig. 1 shows the plot of phase formation based on $\Omega-\delta r$ system, in which the stability of solid solutions, intermetallic compounds and bulk metallic glasses are indicated, as proposed by Yang and Zhang et al. [33]. The calculated coordinates of the five designed HEA model alloys are also added in this map. According to the calculated results shown in Table 2, three alloys HEA-1, HEA-2 and HEA-3, fall into the region of solid solutions with intermetallic compounds (SS+IM), whereas two alloys, HEA-4 and HEA-5, are situated in the subdomain of solid solutions (SS).

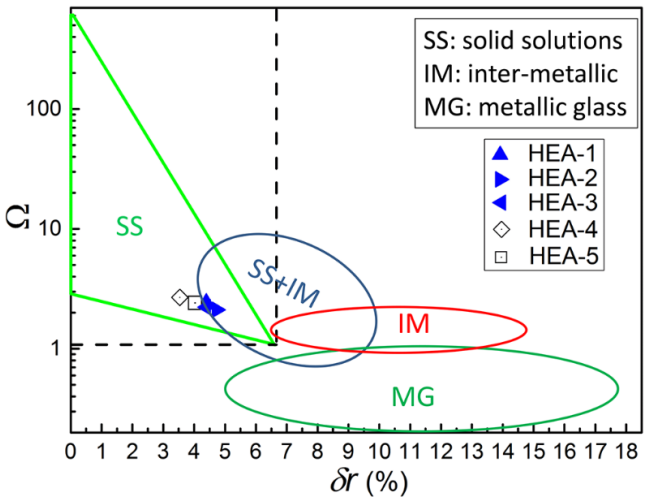

Fig. 1 Phase formation map showing the predicted phase as a function of both the thermodynamic parameter Ω and the atomic size difference δr, as proposed by Yang and Zhang et al. [33]. The coordinates of the HEA model alloys designed for this study are also included. The dashed line represents the region where $\Omega \geq 1.1$, $\delta r \leq 6.6\%$; the green triangle marks the area of reported HEA model alloys with solid solutions.

The chemical composition of HEA-1 is close to the mole formula $Al_{0.3}Cr_{0.9}FeNi_{0.8}$. Therefore, an equilibrium phase calculation based on $Al_XCr_{0.9}FeNi_{0.8}$ (X: 0.05-0.40) has been performed by Thermo-Calc using TCHEA4 database, see results presented in Fig. 2 (a). In case of the phase formed when the alloy is solidified from the liquid phase (cooling rate of arc-melting: ~100 K/s [40-41]), only the solid phases predicted at the upper part of the phase equilibrium diagrams (> 1000 °C) are considered.

The calculation result indicates that HEA-1 will form FCC solid solution, BCC solid solution, and the inter-metallic B2-NiAl phase during solidification.

In case of the other four alloys, an estimated formula of $Al_XCr_{0.68}FeNi$ (X: 0.05-0.40) has been employed to predict the phase compositions during solidification, as shown in Fig. 2 (b). The prediction shows that only FCC phase is solidified from liquid in case of HEA-4 and HEA-5, where the added Al content is x=0.18 and 0.23, respectively. As the amount of Al is increased to x=0.30 (HEA-3), the inter-metallic phase B2-NiAl might form, depending on the exact cooling conditions. HEA-2 with x=0.36, the highest Al content among the candidate alloys, is expected to form FCC, BCC, and B2-NiAl.

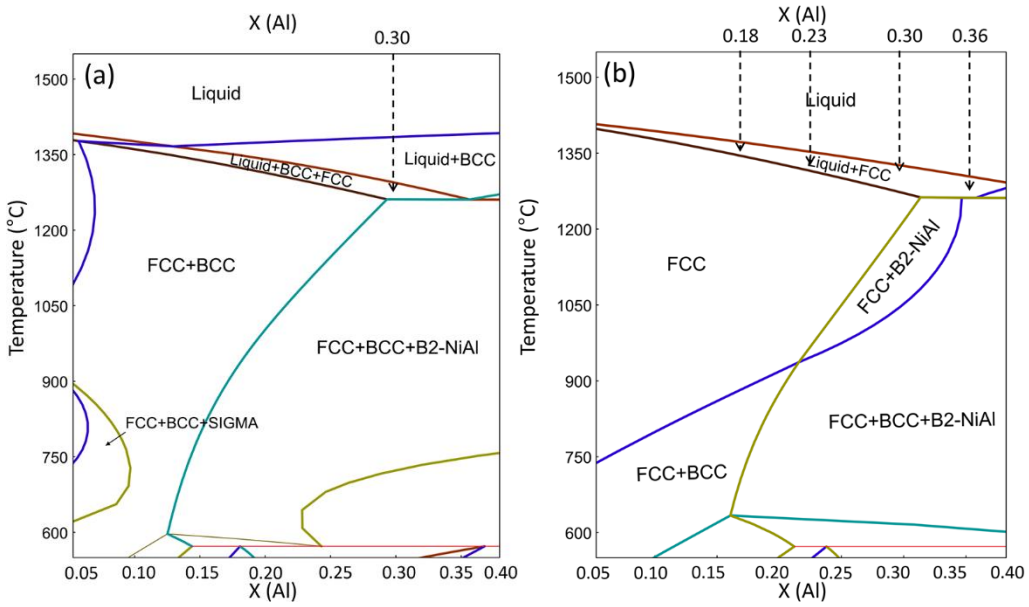

Fig. 2 Equilibrium phase compositions of $Al_XCr_{0.9}FeNi_{0.8}$ (X: 0.05-0.40) (a) and $Al_XCr_{0.68}FeNi$ (X: 0.05-0.40) (b) as a function of Al content X, calculated by Thermo-Calc, TCHEA4 database (FCC: dis-ordered FCC; BCC: dis-ordered BCC; B2-NiAl: ordered BCC; SIGMA: σ-phase); (a) HEA-1 (X(Al): 0.30); (b) HEA-2 (X(Al): 0.36), HEA-3 (X(Al): 0.30), HEA-4 (X(Al): 0.18), HEA-5 (X(Al): 0.23).

3.2 Characterization of as cast alloys

3.2.1 Phase composition

Fig. 3 shows the XRD results of the as cast alloys. HEA-1 and HEA-2 show strong signals from FCC phase while weak signals from B2-NiAl and BCC phases are detected as well. The peaks positions (2θ) of B2-NiAl and BCC phase are clearly separated for the lattice planes of (110) at ~44.5°, (200) at ~ 65°, and (211) at ~ 82°, although the difference is less than 1°. In addition, B2-NiAl phase also has a low angle peak at 2θ=30.96°, (100). Therefore, it is possible to identify these two phases based on X-ray diffraction positions, while it is difficult to mark them separately on the XRD plot figure (Fig. 3). HEA-3, HEA-4 and HEA-5 exhibit X-ray diffraction peaks only from FCC solid solution. The phases identified on each sample are collected and shown in Table 3.

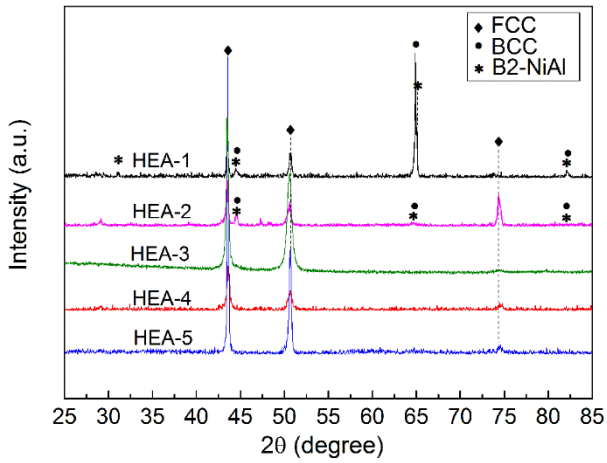

Fig. 3 XRD spectra of as cast HEA model alloys.

Table 3
Phase composition of HEA model alloys in as cast state, measured by XRD.

Sample	Phase composition[1)]		
	FCC (33-397)	B2-NiAl (44-1188)	BCC (34-396)
HEA-1	+	+	+
HEA-2	+	+	+
HEA-3	+	-	-
HEA-4	+	-	-
HEA-5	+	-	-

[1)] PDF no. is given in brackets; +: Yes; -: No.

3.2.2 Microstructure of bulk alloys

Fig. 4 shows representative SEM images of the designed HEA model alloys and Table 4 gives chemical compositions measured by EDS together with nominal compositions.

HEA-1 (Fig. 4 (a)) has formed the typical Widmanstätten lamellae structure. The brighter contrast areas are identified as Ni-rich (see Tab. 4) side plates (labeled N in Fig. 4 (a)), while the interspersed dark large lath layers (labeled IN in Fig. 4 (a)) show Cr-enrichment (Table 4). Concurrent with XRD results (Fig. 3 and Table 3) and as Ni is a FCC stabilizer, the N regions are attributed to the FCC solid solution matrix and the IN regions are assigned to the dis-ordered BCC solid solution, as Cr is a BCC stabilizer.

Additionally, dark-gray appearing precipitates, visible in the higher magnified inset image in Fig. 4 (a), are distributed in the whole alloy matrix. EDS measurements of the precipitates have shown the enrichment of Al and Ni. Therefore, they are assigned to the B2-NiAl phase (ordered BCC).

HEA-2 has formed the dendrite (D) and inter-dendrite (ID) structure in the alloy matrix, shown in Fig. 4 (b). The dendrites, appearing with bright contrast, show a slight depletion in Al and Ni compared with the nominal composition, see Table 4. As they present the dominant phase, they are attributed to the FCC solid solution, which shows the strongest signal in the XRD pattern (Fig. 3). The inter-dendrites are strongly enriched in Al (almost double of nominal composition) and enriched in Ni. Further measurement of the inter-dendrites areas at higher magnification shows the segregation into two morphologies: dark-gray Al- and Ni-rich regions embedded within Fe- and Cr-rich brighter regions. Since B2-NiAl and BCC phases are identified by XRD in addition to the FCC solid solution, the structures of the inter-dendrites are assigned to ordered B2-NiAl (dark-gray regions) and dis-ordered BCC phases (brighter regions within ID). This kind of structure is also reported in $Al_x(CoCrFeNi)_{100-x}$ (x: 8-30 at.%) alloys, which is a result of spinodal decomposition [36, 44-45].

By reducing the amount of Al from 11.7 at.% (in HEA-2) to 9.8 at.% (in HEA-3), the volume fraction of the inter-dendrites decreases, shown in Fig. 4 (c). Nevertheless, the chemical composition of dendrites and inter-dendrites (Table 4) as well as the microstructure of the inter-dendrites (high magnification inset of Fig. 4 (c)) of HEA-3 are comparable with the results of HEA-2. Therefore, it is assumed that B2-NiAl and BCC phases are formed in the inter-dendrites of HEA-3, although these phases are not identified by XRD (most probably due to low fraction in the matrix: < 5 vol.%).

As the Al concentration is further decreased, both HEA-4 and HEA-5 present homogenized morphologies without intermetallic compounds/precipitates (see Fig. 4 (d, e)). The phase composition of alloy matrix is single FCC solid solution according to XRD measurement. The measured chemical compositions are close to the nominal ones, shown in Table 4.

The phase constitutions of designed alloys, identified by XRD and SEM/EDS analysis, are nearly consistent with the prediction results obtained by design rules (Table 1 and Table 2) and thermodynamic calculations (Fig. 2), indicating the applicability of the proposed design approach.

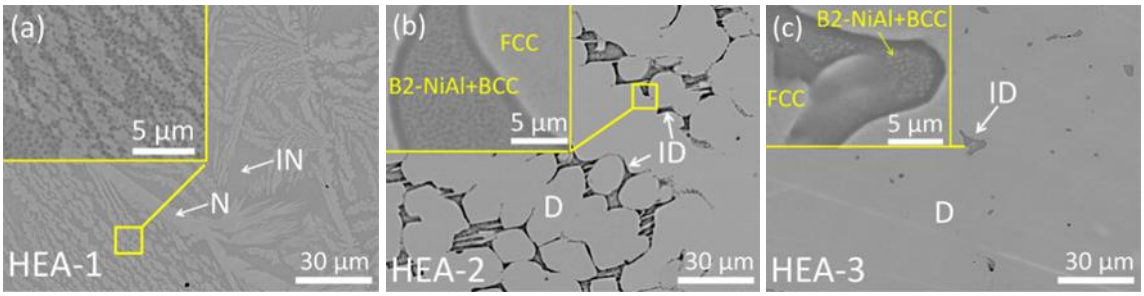

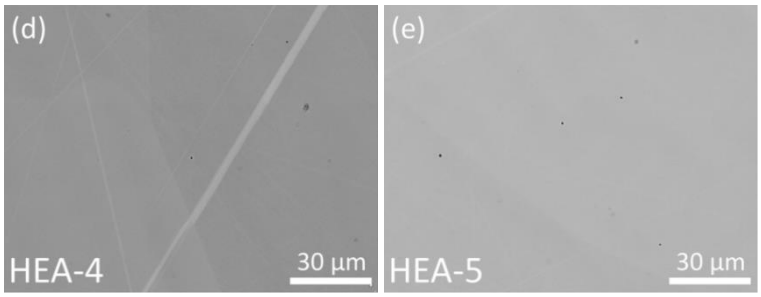

Fig. 4 Representative microstructure of as cast HEA model alloys (HEA-1, HEA-2, HEA-3, HEA-4, HEA-5), N: Ni-rich side plates; IN: interspersed dark lath layers; D: dendrite; ID: inter-dendrite.

Table 4
Chemical compositions of as-cast HEA model alloys, measured by EDS (at.%).

Alloy	Nominal composition (at.%)	Morphology	Al	Cr	Fe	Ni
HEA-1	$Al_{9.8}Cr_{30.3}Fe_{33.0}Ni_{26.9}$	N	6.3	28.8	35.3	29.6
		IN	7.1	33.2	34.6	25.1
HEA-2	$Al_{11.7}Cr_{22.4}Fe_{33.3}Ni_{32.6}$	D	9.3	23.4	36.9	30.4
		ID	20.2	14.1	22.2	43.5
HEA-3	$Al_{9.8}Cr_{22.5}Fe_{33.2}Ni_{34.5}$	D	9.4	23.0	34.5	33.1
		ID	21.0	17.6	21.9	39.5
HEA-4	$Al_{6.0}Cr_{25.0}Fe_{34.0}Ni_{35.0}$	SP	5.8	25.5	34.4	34.3
HEA-5	$Al_{8.0}Cr_{23.2}Fe_{34.0}Ni_{34.8}$	SP	7.9	23.7	34.4	34.0

N: Ni-rich side plates; IN: interspersed dark lath layers; D: dendrite; ID: inter-dendrite; SP: single phase.

3.3 Corrosion behaviour

3.3.1 Phase compositions

Fig. 5 shows the XRD results of the samples after 2000 h exposure at 600 °C. The very weak signals from oxides in combination with diffraction signals from the bulk alloys indicate small thickness of oxide scales. The penetration depth of X-rays can reach up to 5 µm in bulk alloy with Cu Kα1 radiation. According to the characterization results, diffraction signals from spinel-type $(Fe,Cr)_3O_4$, corundum-type Cr_2O_3, corundum-type Al_2O_3, FCC, BCC, B2-NiAl and σ-phase (tetragonal structure) are identified in HEA-1. HEA-2 and HEA-3 show only some of these phases after exposure, namely Cr_2O_3, FCC, B2-NiAl and BCC. In addition, $(Al,Cr)_2O_3$ (Al_2O_3-Cr_2O_3 solid solution) is obtained. The phases identified from exposed HEA-4 include FCC, B2-NiAl plus oxides of Cr_2O_3 and $(Al,Cr)_2O_3$. In case of HEA-5, the phases obtained after exposure are FCC, B2-NiAl and BCC but none of oxide phases.

The identified phase compositions of all exposed samples and the used PDF no. for identification are summarized in Table 5.

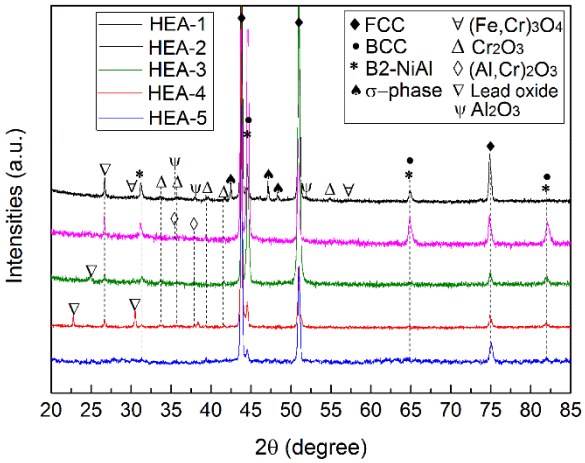

Fig. 5 XRD spectra of HEA model alloys after 2000 h exposure to molten Pb at 600 °C.

Table 5
Phase composition of HEA model alloys after 2000 h exposure to molten Pb, measured by XRD.

Sample	Time (h)	Phase composition[1)] FCC (33-397)	B2-NiAl (44-1188)	BCC (34-396)	Cr_2O_3 (74-326)	$(Al,Cr)_2O_3$ (71-958)	$(Fe,Cr)_3O_4$ (79-418)	Other
HEA-1	2000	+	+	+	+	-	+	Al_2O_3, σ-phase
HEA-2	2000	+	+	+	+	+	-	
HEA-3	2000	+	+	+	+	+	-	
HEA-4	2000	+	+	-	+	+	-	
HEA-5	2000	+	+	-	-	-	-	

[1)] PDF no. is given in brackets; +: Yes; -: No; Al_2O_3 (PDF no. 75-788); σ-phase (PDF no.5-708);

3.3.2 Cross section analysis

HEA-1

Fig. 6 shows the cross section image of HEA-1 after 2000 h exposure. According to the EDS elemental mapping (Fig. 6 (b)), the alloy surface is covered by a continuous oxide layer, non-uniform in thickness. EDS line profiles across a thick part of this layer are shown in Fig. 6 (a). Coinciding signals maxima of O and Cr, together with some Fe are observed at the outer part. The elemental concentrations of this part are consistent with $(Fe,Cr)_3O_4$ (spinel), a phase already identified by XRD. At the inner part of the oxide scale, a narrow region with maximum Al signal coinciding with O signal, indicates the formation of Al_2O_3 scale. The total thickness of the thick oxide scale is up to 0.4 µm. Fig. 6 (c) shows EDS line scan profiles of a thin part of the oxide layer. The signals detected in the oxide scale region are mainly from O and Al. In addition, a weak signal of Cr is identified at the outer surface of the oxide scale. The thickness of the thin oxide scale is around 0.13 µm. Besides, a transitional region between the oxide layer and alloy matrix, characterized with the depletion of oxide former (e.g. Al or-/and- Cr) and enrichment of Fe or-/and- Ni, has formed during oxidation. This layer is usually called transitional layer (TL) [23] and is visible as a bright layer in the SEM image in Fig. 6 (a, b, c). The TL in Fig. 6 (a) shows the enrichment of Fe and depletion in Cr. The formation of Cr rich oxides at the outer layer

leads to Cr depletion, while the Al-rich inner layer impedes the outer diffusion of Fe. The local enrichment of Fe repels the additional Ni, resulting in the low Ni concentration. In the TL of Fig. 6 (c), both Fe and Cr are enriched. Here, the formation of Al-rich thin layer retards the outward diffusion of Cr and Fe, resulting in the cluster of Cr and Fe in TL. In addition, there is an enrichment of Ni and Al at the interface of TL and alloy matrix. This is due to the fact that the line scan performed passes through a B2-NiAl precipitate, shown in dark contrast in the cross sectional image (Fig. 6 (c)).

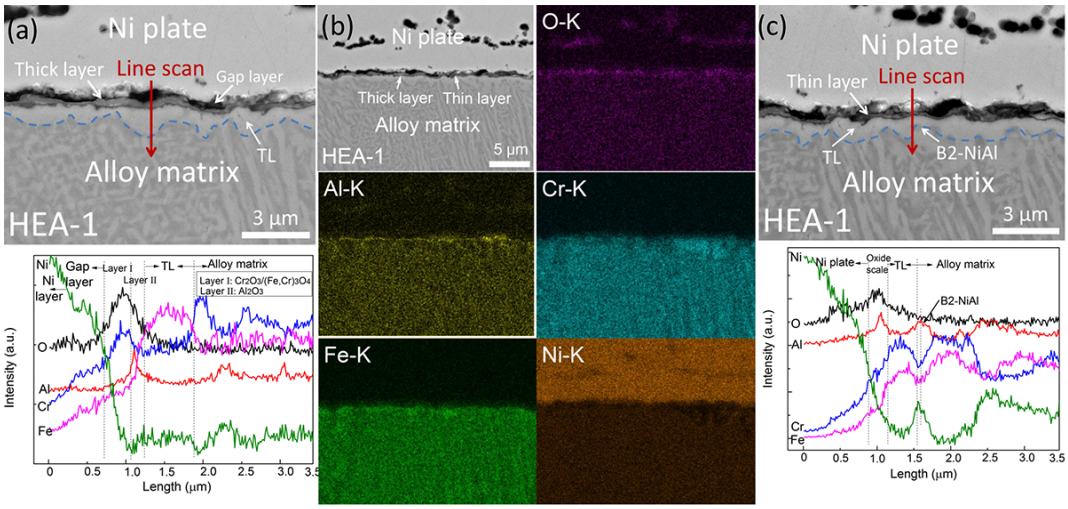

Fig. 6 SEM-EDS analysis of the cross section of HEA-1 after 2000 h exposure to 10^{-6} wt.% oxygen-containing molten Pb at 600 °C, line scan profiles across the thick layer (a); EDS elemental mapping (b); line scan profiles across the thin layer (c); Gap layer: a gap between Ni-layer and oxide scale.

Since the thickness of the oxide layer is less than 0.2 μm in some parts, it is difficult to precisely characterize the microstructure and phase compositions of the oxide scale by XRD and SEM only. Therefore, TEM characterization has been employed to further evaluate the microstructure of the oxide scale.

Fig. 7 presents the TEM bright-field (BF) image and selected area diffraction pattern (SAED) results from the oxide scale. The black circle in Fig. 7 (a) shows the size and position of the selected area aperture. The broad diffraction ring in Fig. 7 (b) stems from the nanocrystalline Pt-coating from the FIB-sample preparation. Fig. 7 (c) is the enlarged image of Fig. 7 (b), which annotates the diffraction spots obtained mainly from the oxide layer. The oxide identified from the diffraction pattern belongs to the corundum-type alumina, shown in Fig. 7 (c). Moreover, the drift-corrected STEM-EDS line profiles along the cross section of the oxide sale are shown in Fig. 7 (d). The oxide scale shows an outer layer with a thickness around 50 nm, and an inner layer with an inverse Winterbottom shape at some regions. The dark contrast region at the interface of inner layer and alloy matrix, which shows the depletion of Al, is a pore formed during the oxide scale growth, which might be further enlarged by ion milling process. Such kind of defect are also observed by Weisenburger et al. [46] and Xu et al. [47].

The strong Cr signal is detected at the outer part of the scale, indicating the formation of Cr_2O_3, while the Al rich inner part indicates the formation of an Al_2O_3 scale. The clear spatial separation of the

Cr and Al signals indicates that Cr_2O_3 and Al_2O_3 do not form a solid solution but are segregated. This is in agreement with the XRD results, which showed respective peaks of Cr_2O_3 and Al_2O_3. The total thickness of the oxide scale is around 80-170 nm, in the same range of the value (around 0.13 µm) measured from SEM image.

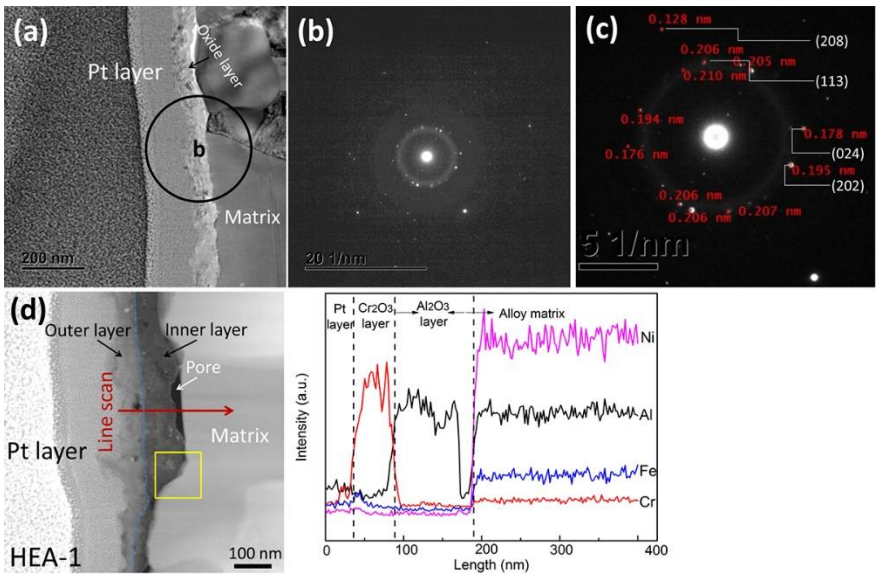

Fig. 7 TEM-BF image of the cross section of HEA-1 and corresponding SAED of oxide scale (a, b, c). The black circle in (a) is highlighting the position of SAED measurement, the full patterns are shown in (b); the enlarged patterns of oxide layer are indexed to be corundum alumina in (c). Drift-corrected STEM-EDS line profiles of the oxide scale formed on HEA-1 after exposure (d). The blue dotted line represents the interface of outer and inner layer, the yellow square represents the reference area for drift correction during acquisition, and the Pt-layer is the protective layer used in FIB sample preparation.

High-resolution TEM images of the outer and inner layer of the oxide scale are shown in Fig. 8 (a) and (b), respectively. By applying Fast Fourier Transformation (FFT), the oxide phases were identified. The lattice plane distances measured at the outer part of the scale (region R1) match the lattice planes of corundum Cr_2O_3, namely (012) and (104) plane, shown in Fig. 8 (a). Measurement at the inner part (Fig. 8 (b)) indicates the formation of corundum Al_2O_3 (lattice plane (113), (202)) at region P1. These results confirm the formation of Cr_2O_3 and Al_2O_3.

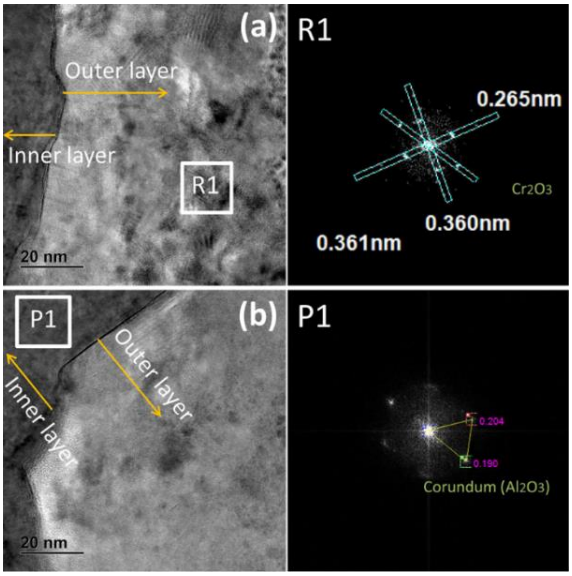

Fig. 8 TEM investigation of HEA-1: HR-TEM image of oxide scale and corresponding FFT image of highlighted area R1 in the outer layer (a); HR-TEM image of oxide scale and corresponding FFT image of highlighted area P1 in the inner layer (b). R1: corundum Cr_2O_3; P1: corundum Al_2O_3.

HEA-2 and HEA-3

Fig. 9 represents the cross-sectional SEM-EDS analysis of HEA-2 after 2000 h exposure. The alloy surface is covered by a thin and continuous oxide layer. According to elemental mapping and line profiles, the signals in the oxide scale region mainly consist of O and Al. The thickness of the oxide scale cannot be measured precisely due to the resolution limit of the SEM image. An estimation of FWHM (full width at half maximum) of the O signal from the EDS line profile indicates that the thickness is less than 0.1 µm (around 90 nm). Besides, some parts, shown in dark contrast with a large thickness (~0.5 µm), are proved as Cr-rich oxides grown into the bulk alloy, see the elemental mapping and line profiles. In addition, a thin TL (~0.5 µm) enriched in Fe (EDS mapping) and depleted in Al, shown in bright contrast, is visible underneath the oxide scale.

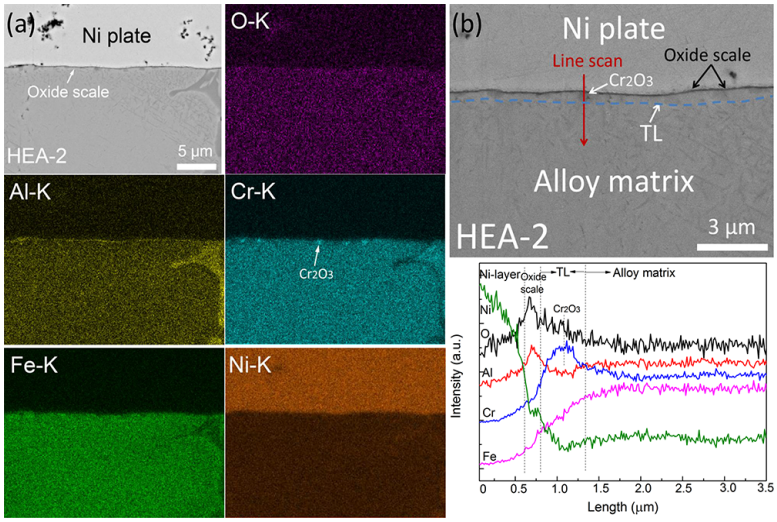

Fig. 9 SEM-EDS analysis of the cross section of HEA-2 after 2000 h exposure to 10^{-6} wt.% oxygen-containing molten Pb at 600 °C, EDS elemental mapping (a); EDS line scan profiles (b).

TEM-results of HEA-2 are summarized in Fig. 10. The oxide layer is indicated by the arrow in Fig. 10 (a). The SAED of the oxide scale (shown in Fig. 10 (b) and measured at the position marked with a white circle in (a)) shows the electron diffraction patterns. The ring patterns stem from the amorphous Pt-coating, as explained in Fig. 7. Besides, some spots distributed around the ring patterns are diffractions from oxide scale, which might also indicate the formation of nano-crystalline oxides. The identified diffraction patterns are indexed to the corundum alumina. The thickness of oxide scale is around 0.1 µm. Moreover, a STEM-EDS line scan has been performed through the oxide scale of HEA-2, shown in Fig. 10 (c). A uniform oxide scale shown in dark contrast covers the alloy surface. According to the analysis, the dense oxide layer shows the enrichment of Cr at the outer part while Al is enriched at the inner part. However, in contrast to HEA-1, where a segregation of Cr_2O_3 and Al_2O_3 was observed, HEA-2 shows signals from Al and Cr at the outer surface scale, indicating a mixed Cr_2O_3-Al_2O_3 oxide layer. This measurement agrees with the results from XRD, which showed the formation of an $(Al,Cr)_2O_3$ solid solution. In addition, some oxides branches grown above the surface are also visible, as well as a slight enrichment of Fe at the surface of the oxide layer. The needle-like oxide branches, mainly enriched in Al, can be γ-Al_2O_3, which is formed during the early stage of oxidation [48].

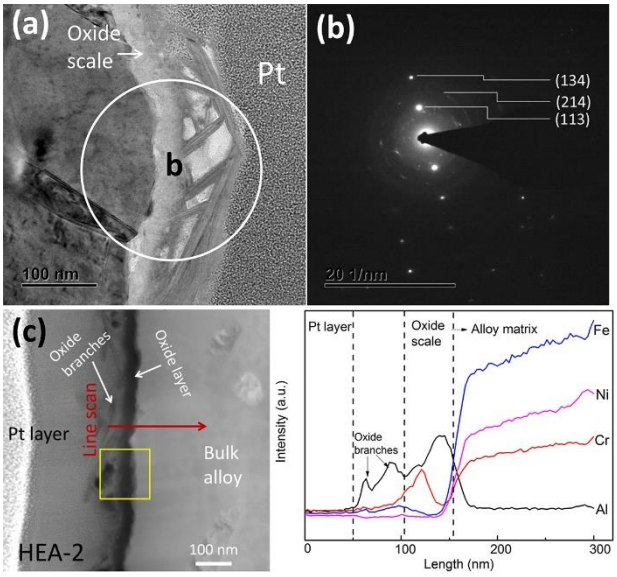

Fig. 10 TEM-BF images of the cross section of HEA-2 and corresponding SAED of oxide scale (a, b). The white circle in (a) is highlighting the position of SAED measurement, the patterns are indexed to be corundum alumina in (b). Drift-corrected STEM-EDS line profiles of the oxide scale formed on HEA-2 after exposure (c). The yellow square represents the reference area for drift correction during acquisition, and the Pt-layer is the protective layer used in FIB sample preparation.

HEA-3 shows a corrosion behaviour similar to HEA-2. The respective results are presented in the supplemental material.

HEA-4 and HEA-5

The cross section of the oxide scale formed on HEA-4 is presented in Fig. 11. According to the EDS elemental mapping and line scan, the oxide scale is mainly enriched in O, Al and Cr, where the Cr signal coincides with the Al signal or is slightly in front of the Al signal, see line profiles (Fig. 11 (b)). The thickness of the oxide scale is around 0.14 µm. Besides, a bright Ni- and Fe-rich TL layer, depleted in Al and Cr, with a thickness around 2.5 µm, is observed below the oxide scale, shown in Fig. 11 (b). Moreover, some Cr-rich precipitates, distributed in the TL, are also identified. The precipitation of Cr-rich compounds might be caused by the elemental diffusion during oxidation, which is also observed in alumina-forming austenitic (AFA) alloys after exposure to oxygen-containing molten Pb [22, 24].

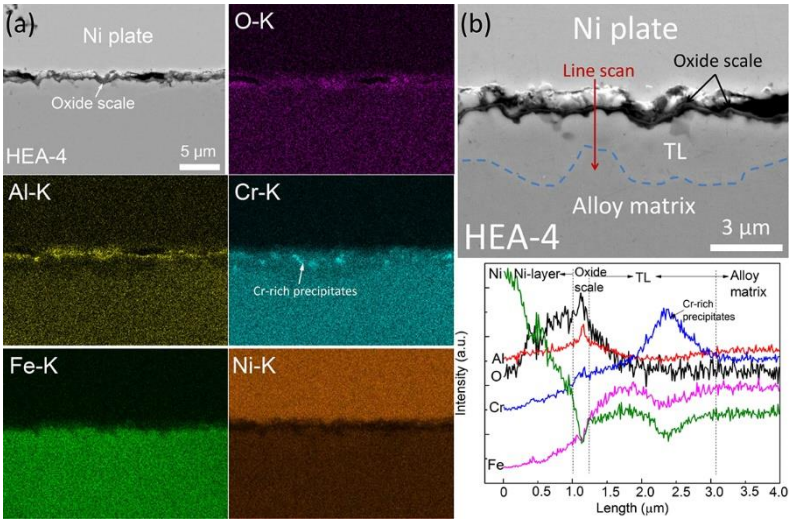

Fig. 11 SEM-EDS analysis of the cross section of HEA-4 after 2000 h exposure to 10^{-6} wt.% oxygen-containing molten Pb at 600 °C, EDS elemental mapping (a); EDS line scan profiles (b).

Regarding the HEA-5, although the oxide scale partially spalled off during/after extraction of the specimen from the molten Pb, analysis of the remaining alloy did not show any corrosion attack, see supplemental material. From these results, it is concluded that indeed a protective scale had formed similar to the single-phase alloy HEA-4.

3.4 Microstructure evolution

Microstructure stability during service is quite essential for structural materials under loading at high temperature [10, 27, 49-50]. Therefore, the microstructure of HEA model alloys after 2000 h exposure at 600 °C has been characterized.

Two main points are considered for the microstructure evaluation: (I) phase transformation; (II) precipitation.

Representative SEM images of HEA model alloys HEA-1, HEA-2 and HEA-4 are presented in Fig. 12. The morphology of HEA-1 displays a lamellar microstructure plus distributed dark-gray precipitates in the alloy matrix, which is consistent with the as cast alloy (Fig. 4) and the phases FCC, BCC and B2-NiAl identified by XRD after exposure, see Fig. 5 and Table 5. In addition, low amount of σ-phase (low peak

intensity) has been detected by XRD, which is in accordance to the predictions by equilibrium phase calculations. According to the equilibrium phase calculation shown in Fig. 12 (b), the phase constitution of HEA-1 at 600 °C includes 47.8 mole % FCC, 25.0 mole% BCC, 21.2 mole% B2-NiAl (ordered BCC) and 6.0 mole% σ-phase. However, the σ-phase is difficult to be recognized from SEM images due to the complex morphology in the alloy matrix. The precipitates of σ-phase after thermal aging, mostly observed at 500-700 °C, are reported in $Al_xCoCrFeNi$ (x from 0.4 to 1.2) [36, 51-52], $Al_{0.5}CoCrCuFeNi$ [53], CoCrFeMnNi [54]. In general, the interfaces of FCC/BCC, B2/BCC and grain boundaries are considered as the easiest regions for σ-phase nucleation because of the high boundary energy [36, 54-56].

Fig. 12 (c) shows the morphology in the bulk alloy of HEA-2 after exposure. The dendrite and inter-dendrite structures, which consist of an FCC phase matrix plus conjoint B2-NiAl and BCC secondary phase, are maintained during exposure. However, acicular precipitates, which are adjacent to the dendrites, have been observed after 2000 h exposure. Such kinds of precipitates are also observed in the vicinity to the grain boundaries of $Al_{0.3}CoCrFeNi$ alloy after thermal aging at 900 °C [57], and in the FCC matrix of $Al_{0.5}CoCrFeNi$ after aging at 900-1100 °C [51], which are proved as B2-NiAl phase by TEM [51, 57-58]. Equilibrium phase calculation also predicts the existence of B2-NiAl phase. The calculated phase composition of HEA-2 at 600 °C shows the composition of 57.4 mole% FCC, 18 mole% BCC and 24.6 mole% B2-NiAl, see Fig. 12 (d). HEA-3 has shown the same microstructure as HEA-2 after exposure.

The single phase alloy HEA-4 is able to preserve the FCC alloy matrix during exposure. However, precipitation of B2-NiAl, which is confirmed by XRD and EDS analysis, has been observed along the grain boundaries, see the dark precipitates in Fig. 12 (e). Gwalani et al. [59] also reported the precipitates of B2-NiAl phase along grain boundaries of $Al_{0.3}CoCrFeNi$ after thermal aging at 620 °C for 50 h. Equilibrium phase calculation of HEA-4 shows the formation of 18 mole% B2-NiAl in the FCC alloy matrix (including ordered FCC) at 600 °C, displayed in Fig. 12 (f). HEA-5 has shown the same microstructure as HEA-4 after exposure.

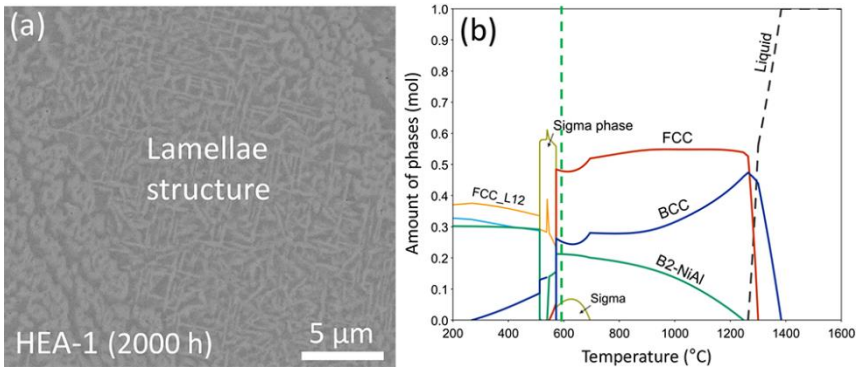

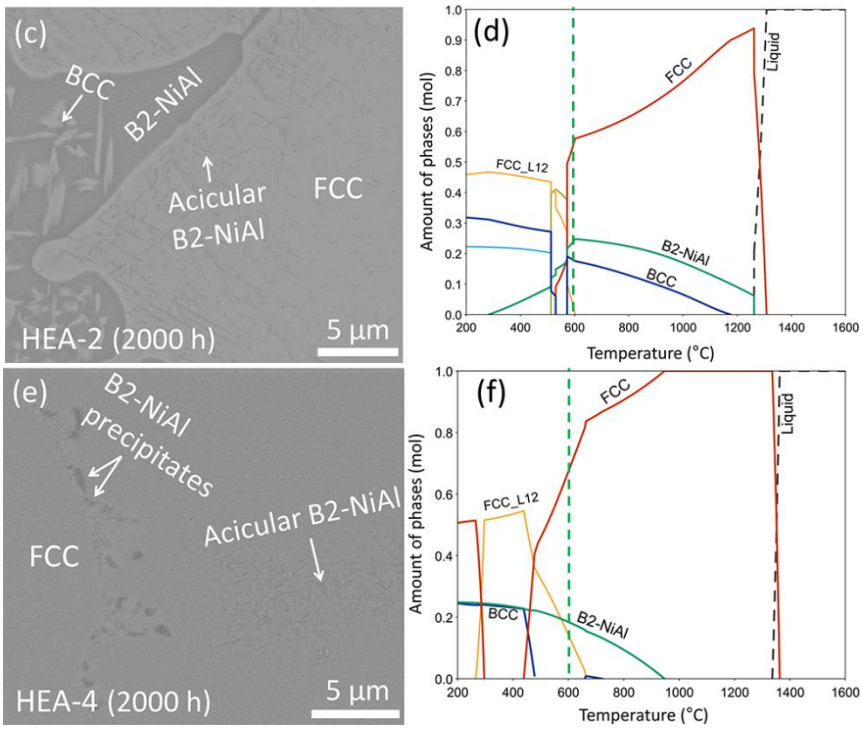

Fig. 12 SEM images of the alloy matrix after 2000 h exposure at 600 °C, (a) HEA-1, (c) HEA-2, (e) HEA-4; and equilibrium phase calculation performed by Thermo-Calc with the database TCHEA4, (b) HEA-1, (d) HEA-2, (f) HEA-4; (FCC_L12: ordered FCC).

4. Discussion

Using empirical parameters (ΔH_{mix}, *VEC*, δr and Ω) and thermo-dynamic modeling, design and prediction of phase compositions for AlCrFeNi-based HEA model alloys is successful. The as cast HEA-1 ($Al_{9.76}Cr_{30.28}Fe_{32.95}Ni_{26.91}$) with a low *VEC* value (7.44) has formed a dual-phase structure of FCC and BCC with Al-, and Ni-rich B2-type precipitates dispersed in the matrix. This is mainly due to the fact that the concentrations of all BCC-stabilizers (Al, Cr and Fe) are not totally compensated by the concentration of FCC-stabilizer (Ni) [60]. Although BCC phase is also formed in HEA-2, it is due to the spinodal decomposition of B2-NiAl phase within the IDs. The formation of B2-NiAl inter-metallic compounds in HEA-1, HEA-2 and HEA-3 is mainly due to the high amount of Al addition, which is beyond the solubility limit of Al in the solid solution (FCC or BCC) matrix (the measured Al concentration in FCC matrix of HEA-2 and HEA-3 is around 9.3 at.%, see Table 4). Alloying element Al has played the determining role on secondary B2-NiAl phase formation in the Al-Cr-Fe-Ni system, which is also reported in AlCrFeCoNi HEAs [50-52]. The relatively low enthalpy of formation of B2-NiAl (-22 kJ/mol calculated by Miedema's model [61]) promotes the formation of B2-NiAl phase during solidification. Moreover, the morphology of B2-NiAl secondary phase, either in terms of small precipitate or dendrite/inter-dendrite, is also significantly influenced by the amount of Al addition.

4.1 Oxidation mechanism of Al-Cr-Fe-Ni

Double-layer/bi-layer structure is the main feature of the oxide scale passivating the HEA model alloys when exposed to oxygen-containing molten Pb environment. Basically, there are two types of

double oxide layers formed on HEA-1 during exposure at 600 °C. One type is based on outer $(Fe,Cr)_3O_4$/inner Al_2O_3 bi-layer, and the other type is outer Cr_2O_3/inner Al_2O_3 bi-layer. The explanation is related to the microstructure of alloy matrix since FCC and BCC phases exhibit different oxidation behaviour [62]. As observed by Jepson et al. [62], the thick oxide layer formed on BCC phase is Fe-rich oxide while the thin layer formed on FCC phase is Cr-rich oxide despite the existence of Mn-rich oxide on both phases. The reason for this difference is the faster diffusion of alloying elements in BCC than in FCC phase [62-63]. The formation of spinel or spinel/alumina layer is observed in other Al-containing HEAs, namely the oxidation of $Al_{0.4}CoCrFeNi$ in supercritical water at 600 °C [64], oxidation of $Al_{0.6}CrFeCoNi$ in air at 800 to 1000 °C [65].

Regarding the growth mechanism of Cr_2O_3-Al_2O_3 based oxide scale in our experimental conditions, no available data can be cited. Most of the literatures are focused on the oxidation of alumina-forming alloys above 1000 °C in air or in pure oxygen atmosphere [66-70]. It is commonly agreed that alumina scale formation above 1000 °C is related to the countercurrent inward diffusion of oxygen and outward diffusion of aluminum [70-75]. However, the oxidation mechanism at lower temperature and reduced oxygen concentration can be different.

The schematic diagram of Fig. 13 describes the process of oxide scale formation on HEA model alloys either with FCC or FCC plus BCC solid solutions. At the initial stage of the exposure (oxidation), all of the alloying elements will be oxidized to form a thin layer with multiple oxides [76]. This initial thin layer retards the outward diffusion of alloying elements and inward permeation of oxygen, resulting in the reduced oxygen activity at the interface of initial layer/alloy matrix. Consequently, selective oxidation of alloying elements, mainly Cr and Al because of their high oxygen affinity [77-78], occurs on the metal surface, representing the second transient stage of oxidation. Here, Cr is preferentially being oxidized in FCC solid solution to form a continuous layer because of its higher concentration in bulk alloy, the faster mobility of Cr compared to Al in FCC phase (due to smaller atom size), and the higher growth rate of Cr_2O_3 [77, 79-80]. In case of BCC solid solution, Fe is also being oxidized together with Cr to form $(Fe,Cr)_3O_4$ because of the high diffusion coefficients of Fe atoms in BCC phase [64-65]. During this stage, the oxidation is controlled by countercurrent inward diffusion of oxygen and outward diffusion of Cr or-/and- Fe. As the thickness of Cr_2O_3 or $(Fe,Cr)_3O_4$ layer increases, the outward diffusions of alloying elements like Cr and Fe become difficult while the inward diffusion of oxygen dominates the process. Accordingly, the new oxide is preferentially nucleated at the interface of oxide layer/alloy matrix. Since the oxygen partial pressure is low at inner side of the scale, only the most active elements like Cr and Al are oxidized [47]. Moreover, the corundum crystalline structure of Cr_2O_3 also provides nucleation site for α-Al_2O_3 (corundum) which results in the formation of $(Al,Cr)_2O_3$ solid solutions, as identified in this study. As the Cr_2O_3/$(Al,Cr)_2O_3$ bi-layer becomes even thicker, the further reduced oxygen activity only allows Al being oxidized because of the lowest oxygen dissociation partial pressure of Al_2O_3 [12, 47, 81-82]. The formation of segregated Cr_2O_3 and Al_2O_3 layers represents the end of the transient stage of oxidation, and the start of the steady-state of oxidation. During the steady stage oxidation, the oxidation rate is significantly reduced because of the slow growth of Al_2O_3.

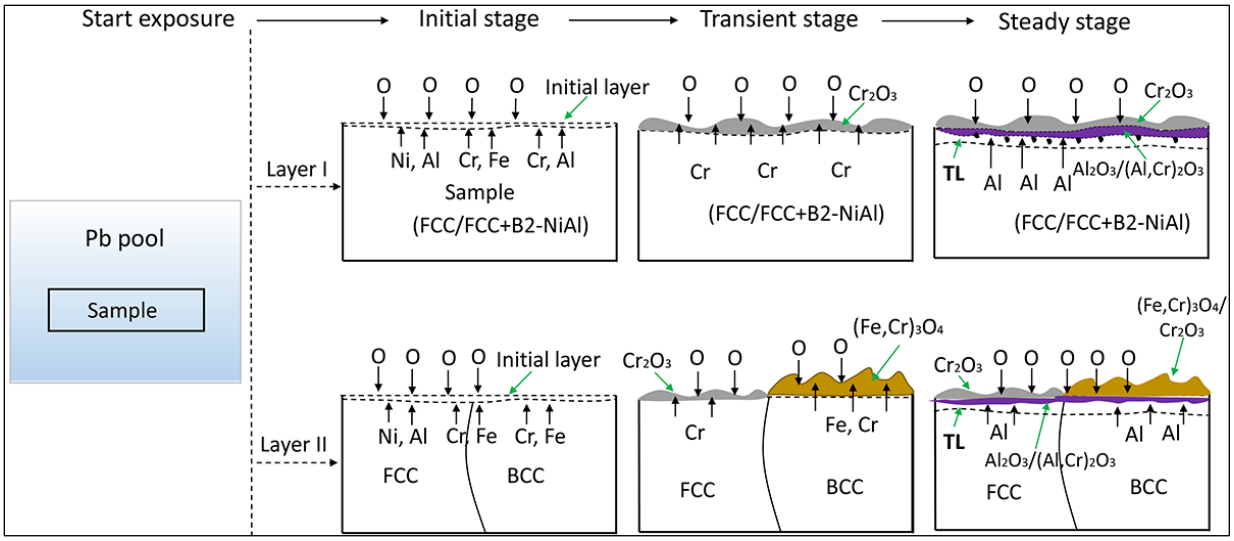

Fig. 13 Schematic diagram of the oxide scale formed on designed HEA model alloys when exposed to oxygen containing molten Pb at 600 °C; grey color: Cr_2O_3 layer, violet color: Al_2O_3 or $(Al,Cr)_2O_3$ layer, yellow color: $(Fe,Cr)_3O_4$ layer; the black arrow indicates the diffusion of elements.

4.2 Thickness of oxide scale and TL

Table 6 collects the thickness of oxide scale formed on each sample. The thickness of $(Fe,Cr)_3O_4/Al_2O_3$ bi-layer is 3 to 4 times thicker than the $Cr_2O_3/(Al,Cr)_2O_3$ bi-layer, mainly due to the fast growth of the outer $(Fe,Cr)_3O_4$ layer [47, 62], while the Al_2O_3 layer formed underneath the $(Fe,Cr)_3O_4$ layer inhibits the outward diffusion of Cr and Fe. Compared with $(Fe,Cr)_3O_4$ spinel/Al_2O_3 bi-layer, $Cr_2O_3/(Al,Cr)_2O_3$ or Cr_2O_3/Al_2O_3 bi-layer has shown a relatively low growth rate during the corrosion tests.

Table 6
Thickness of oxide scale formed on HEA model alloys after 2000 h exposure to oxygen-containing molten Pb at 600 °C.

	HEA-1	HEA-2	HEA-3	HEA-4
Oxide scale thickness (μm)	thin part ($Cr_2O_3/(Al,Cr)_2O_3$): 0.13 thick part ($(Fe,Cr)_3O_4/Al_2O_3$): 0.4	0.1	0.12	0.14

In addition, a transitional layer (TL) underneath the oxide scale, with the characteristics of a slight depletion of Al and Cr, enrichment of Fe or-/and- Ni, and some B2-NiAl and Cr-rich precipitates, have been recognized and defined. As depicted in Fig. 6, 9 and 11, the TL formed on HEA-1 and HEA-2 is slightly different from that of HEA-3 and HEA-4. The B2-NiAl precipitates observed in the matrix of HEA-1 and HEA-2 are consumed in the TL, which acts as Al-reservoir during the oxidation process. Therefore, less depleted zone of Al contributes to the thinner TL formed on HEA-1 and HEA-2. Moreover, the enrichment of Fe also proves the role of alumina layer acting as an efficient diffusion barrier. Regarding the precipitates observed in the TL of HEA-4 and HEA-5, this is mainly due to the diffusion of Cr towards the surface during the transient stage of oxidation. Then the local enrichment of Al and Ni results in the B2-NiAl phase formation. On the other hand, the formation of B2-NiAl phase repels Cr, due to the low

solubility of Cr in stoichiometric NiAl phase [83] and will cause the surrounding areas further enriched in Cr [84], as we can see in Fig. 9 and Fig. 11.

Fig. 14 displays the relations of the thickness of oxide scale and TL by varying the Al content in HEA-2, HEA-3 and HEA-4. A nearly linear decrease of the oxide scale thickness with the Al content is obtained. The thicknesses of TL is also decreased as the amount of Al increases, shown also in Fig. 14. Since a high amount of Al addition promotes the formation of alumina, which grows slower compared with chromia layer, the oxide layer formed on samples with higher Al concentration becomes thinner. The observed TL is a result of depletions of Al and Cr during oxidation, more pronounced in Cr consumption. Therefore, the thinner the oxide scale, the less Cr is consumed and thus the thinner TL as well.

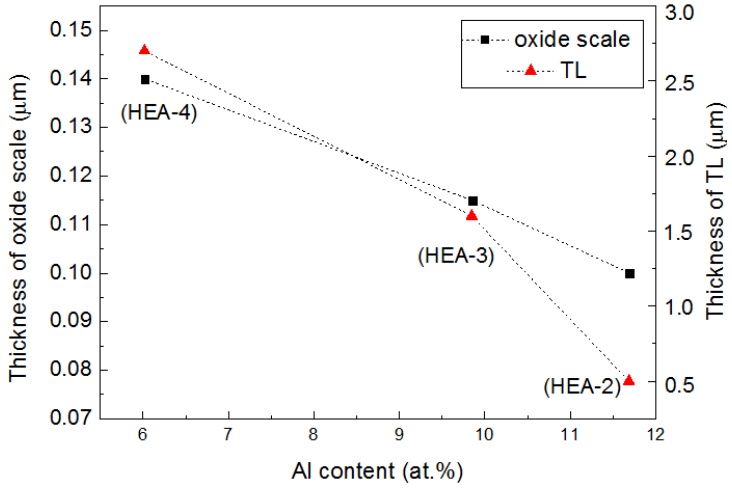

Fig. 14 Plot of relation between the thickness of oxide scale and TL as a function of Al content of the exposed HEA model alloys (HEA-2, HEA-3, HEA-4).

4.3 Microstructure stability after thermal aging

The microstructure of HEA-1 shows the formation of small amount of σ-phase after 2000 h exposure at 600 °C. Possible explanations for the σ-phase formation include the high amount of Cr addition, which is a strong σ-phase former in binary alloying systems like Cr-Fe, Cr-Ni promoting the σ-phase formation [45, 55]. Regarding the alloys HEA-2 and HEA-3, acicular B2-NiAl precipitates are the main feature of phase evolution after exposure. It is found that the rod-shaped B2-NiAl precipitates directly nucleate from FCC matrix because of the observed Kurdjumov–Sachs (K–S) relationship in crystal orientations [57]. However, the precipitates do not degrade the stress-strain properties of bulk alloy [57].

Both HEA-4 and HEA-5 have preserved the FCC alloy matrix during exposure. In addition, B2-NiAl precipitates have formed along the grain boundaries of both alloys. The B2-NiAl phase is a brittle intermetallic compound, which increases the strength of base alloy at the cost of ductility [85]. However, by careful controlling the size and distribution of B2-NiAl precipitates, superior mechanical properties of the bulk alloy can be achieved. For instance, Liu et al. [85] reported the improved yield stress of $Al_{0.3}$CoFeCrNi with contributions partly from B2-NiAl precipitates. Nguyen et al. [86] have presented the

superplastic deformation behaviour of $Al_9(CoCrFeMnNi)_{91}$ with B2-NiAl precipitates. Gwalani et al. [59, 87], and Choudhuri et al. [88] made heat treatment of $Al_{0.3}CoCrFeNi$ to achieve a combination of excellent strength and ductility by precipitation of B2-NiAl phase along grain boundaries. The presence of B2-NiAl phase prevents the grain growth and displays precipitation hardening during deformation. This leads to the excellent mechanical properties of Al-containing HEAs [85-88].

HEA model alloys show corrosion/oxidation features similar to that of AFA alloys when exposed to molten Pb, e.g. thin oxide layer, oxides of Cr_2O_3, Al_2O_3-Cr_2O_3 solid solution, TL [12, 22, 24]. However, compared with AFA alloys, the designed HEA model alloys are even more corrosion resistant at 600 °C. For example, small regions with local dissolution attack are observed in some AFA alloys exposed to molten Pb at 550 to 650 °C [22-24], even though the alloys are generally corrosion resistant. But no such kind of corrosion attack is observed on HEA model alloys. In addition, additional types of oxides, like magnetite protrusions and $Fe(Cr,Al)_2O_4$ type spinel precipitates, have been observed on AFA alloys [23-24]. Again, these features are not observed on HEA model alloys. That means a more uniform oxide layer has developed on HEA model alloys. The experimental results also indicate that even with a relative high Ni content, it is still possible to avoid the risk of dissolution attack by forming an efficient and protective oxide scale. This will help enlarge the range for searching for HEAs that might show their superior properties in aggressive conditions targeting for commercial applications. Further study of HEA properties in more aggressive conditions and higher temperatures would be more interesting to show the advantages of these HEAs when compared with AFA alloys.

5. Conclusion

Five AlCrFeNi HEA model alloys have been designed, exposed to aggressive molten Pb, and characterized to investigate their applicability for high temperature environments. The relationship of phase compositions and properties (corrosion, microstructure stability) has been discussed. Based on the results, the main conclusions can be given as following:

(a) The empirical parameters (ΔH_{mix}, δr, VEC and Ω) combined with thermo-dynamic phase calculation can be used for HEA design and phase predication.

(b) Four samples exhibit excellent corrosion resistance by forming protective oxide scale based on $(Fe,Cr)_3O_4/Al_2O_3$ bi-layer or-/and- $Cr_2O_3/(Al,Cr)_2O_3$ bi-layer. One sample ($Al_{0.23}Cr_{0.68}FeNi_{1.02}$) shows the evidence of oxide scale exfoliation after corrosion test (during cooling).

(c) The thickness of $Cr_2O_3/(Al,Cr)_2O_3$ bi-layer and transitional layer (TL) is decreased as the amount of Al addition increases. A nearly linear decrease is obtained between the oxide scale thickness and Al content.

(d) Sample $Al_{0.30}Cr_{0.92}FeNi_{0.82}$ has formed σ-phase in the bulk alloy after 2000 h exposure at 600 °C. One sample ($Al_{0.36}Cr_{0.67}FeNi_{0.98}$) with FCC plus IDs, and two alloys ($Al_{0.18}Cr_{0.73}FeNi_{1.03}$, $Al_{0.23}Cr_{0.68}FeNi_{1.02}$) with single FCC alloy matrix are able to maintain the microstructure during exposure. Sample $Al_{0.30}Cr_{0.68}FeNi_{1.04}$ shows the increased volume of IDs (B2-NiAl+B2) during exposure. Moreover, B2-NiAl precipitates are observed along grain boundaries (GBs) of single FCC phase alloys, and acicular B2-NiAl precipitates adjacent to IDs or GBs are visible in four alloys (except $Al_{0.30}Cr_{0.92}FeNi_{0.82}$) after

exposure. The phases compositions observed from experiments are consistent with equilibrium phase calculations.

Data availability

The raw/processed data required to reproduce these findings cannot be shared at this time due to technical or time limitations.
The datasets obtained during the current study are available from the corresponding author on reasonable request.

Acknowledgements

This work was supported by the Helmholtz program NUSAFE at the Karlsruhe Institute of Technology and has been carried out in the frame of EERA Point Programme of Nuclear Materials, partly funded by the European Commission HORIZON 2020 Framework Programme under grant agreement No. 755269. We acknowledge the Karlsruhe Nano Micro Facility (KNMF), a Helmholtz Research infrastructure, for providing access to TEM and FIB technology (Proposal number 2018-021-024429). Hao Shi appreciates the Postdoc fellowship jointly funded by Helmholtz-OCPC Program (No. 20191028).

Appendix A. Supplementary data

Supplementary material for this article can be found online at xxx.

Reference

[1] A.J. Carrillo, J. González-Aguilar, M. Romero, J.M. Coronado, Solar energy on demand: A review on high temperature thermochemical heat storage systems and materials, Chem. Rev. 119 (2019) 4777-4816. https://doi.org/10.1021/acs.chemrev.8b00315.

[2] J.E. Kelly, Generation IV International Forum: A decade of progress through international cooperation, Prog. Nucl. Energy 77 (2014) 240-246. https://doi.org/10.1016/j.pnucene.2014.02.010.

[3] F. Roelofs, B. de Jager, A. Class, H. Jeanmart, P. Schuurmans, A. Ciampichetti, G. Gerbeth, R. Stieglitz, C. Fazio, European research on HLM thermal hydraulics for ADS applications, J. Nucl. Mater. 376 (2008) 401-404. https://doi.org/10.1016/j.jnucmat.2008.02.014.

[4] V. Coen, Lithium-lead eutectic as breeding material in fusion reactors, J. Nucl.Mater. 133 (1995) 46-51. https://doi.org/10.1016/0022-3115(85)90110-2.

[5] A. Abánades, R.K. Rathnam, T. Geißler, A. Heinzel, K. Mehravaran, G. Müller, M. Plevan, C. Rubbia, D. Salmieri, L. Stoppel, S. Stückrad, Development of methane decarbonisation based on liquid metal technology for CO_2-free production of hydrogen, Int. J. Hydrog. Energy 41 (2016) 8159-8167. https://doi.org/10.1016/j.ijhydene.2015.11.164.

[6] H. Kim, D.A. Boysen, J.M. Newhouse, B.L. Spatocco, B. Chung, P.J. Burke, D.J. Bradwell, K. Jiang, A.A. Tomaszowska, K. Wang, W. Wei, Liquid metal batteries: past, present, and future., Chem. Rev. 113 (2013) 2075-2099. https://doi.org/10.1021/cr300205k.

[7] M. Sarvghad, S.D. Maher, D. Collard, M. Tassan, G. Will, T.A. Steinberg, Materials compatibility for the next generation of Concentrated Solar Power plants, Energy Storage Mater. 14 (2018) 179-198. https://doi.org/10.1016/j.ensm.2018.02.023.

[8] U. Pelay, L. Luo, Y. Fan, D. Stitou, M. Rood, Thermal energy storage systems for concentrated solar power plants, Renew. Sustain. Energy Rev. 79 (2017) 82-100. https://doi.org/10.1016/j.rser.2017.03.139.

[9] S.J. Zinkle, G.S. Was, Materials challenges in nuclear energy, Acta Mater. 61 (2013) 735-758. https://doi.org/10.1016/j.actamat.2012.11.004.

[10] K.L. Murty, I. Charit, Structural materials for Gen-IV nuclear reactors: Challenges and opportunities, J. Nucl. Mater. 383 (2008) 189-195. https://doi.org/10.1016/j.jnucmat.2008.08.044.
[11] H. Shi, Alumina forming alloys (steels, high entropy materials) for the mitigation of compatibility issues with liquid metals and steam in energy related, high-temperature applications, Karlsruher Institut für Technologie (KIT), Karlsruhe, 2020. DOI: 10.5445/IR/1000105453.
[12] C. Fazio, V.P. Sobolev, A. Aerts, S. Gavrilov, K. Lambrinou, P. Schuurmans, A. Gessi, P. Agostini, A. Ciampichetti, L. Martinelli, S. Gosse, Handbook on lead-bismuth eutectic alloy and lead properties, materials compatibility, thermal-hydraulics and technologies-2015 edition (No. NEA--7268), Organisation for Economic Co-Operation and Development, 2015.
[13] J. Pacio, T. Wetzel, Assessment of liquid metal technology status and research paths for their use as efficient heat transfer fluids in solar central receiver systems, Sol. Energy 93 (2013) 11-22. https://doi.org/10.1016/j.solener.2013.03.025.
[14] D. Frazer, E. Stergar, C. Cionea, P. Hosemann, Liquid metal as a heat transport fluid for thermal solar power applications, Energy Procedia 49 (2014) 627. https://doi.org/10.1016/j.egypro.2014.03.068.
[15] R.G. Ballinger, J. Lim, An overview of corrosion issues for the design and operation of high-temperature lead-and lead-bismuth-cooled reactor systems, Nucl. Technol 147 (2004) 418-435. https://doi.org/10.13182/NT04-A3540.
[16] C. Schroer, O. Wedemeyer, J. Novotny, A. Skrypnik, J. Konys, Selective leaching of nickel and chromium from Type 316 austenitic steel in oxygen-containing lead–bismuth eutectic (LBE), Corros. Sci. 84 (2014) 113-124. https://doi.org/10.1016/j.corsci.2014.03.016.
[17] J. Zhang, N. Li, Review of the studies on fundamental issues in LBE corrosion, J. Nucl. Mater. 373 (2008) 351-377. https://doi.org/10.1016/j.jnucmat.2007.06.019.
[18] A. Weisenburger, C. Schroer, A. Jianu, A. Heinzel, J. Konys, H. Steiner, G. Müller, C. Fazio, A. Gessi, S. Babayan, A. Kobzova, Long term corrosion on T91 and AISI1 316L steel in flowing lead alloy and corrosion protection barrier development: Experiments and models, J. Nucl. Mater. 415 (2011) 260-269. https://doi.org/10.1016/j.jnucmat.2011.04.028.
[19] J. Van den Bosch, R.W. Bosch, D. Sapundjiev, A. Almazouzi, Liquid metal embrittlement susceptibility of ferritic–martensitic steel in liquid lead alloys, J. Nucl. Mater. 376 (2008) 322-329. https://doi.org/10.1016/j.jnucmat.2008.02.008.
[20] G. Müller, G. Schumacher, F. Zimmermann, Investigation on oxygen controlled liquid lead corrosion of surface treated steels, J. Nucl. Mater. 278 (2000) 85-95. https://doi.org/10.1016/S0022-3115(99)00211-1.
[21] G. Müller, A. Heinzel, G. Schumacher, A. Weisenburger, Control of oxygen concentration in liquid lead and lead–bismuth, J. Nucl. Mater. 321 (2003) 256-262. https://doi.org/10.1016/S0022-3115(03)00250-2.
[22] H. Shi, A. Jianu, A. Weisenburger, C. Tang, A. Heinzel, R. Fetzer, F. Lang, R. Stieglitz, G. Müller, Corrosion resistance and microstructural stability of austenitic Fe–Cr–Al–Ni model alloys exposed to oxygen-containing molten lead, J. Nucl. Mater. 524 (2019) 177-190. https://doi.org/10.1016/j.jnucmat.2019.06.043.
[23] J. Ejenstam, P. Szakalos, Long term corrosion resistance of alumina forming austenitic stainless steels in liquid lead, J. Nucl. Mater. 461 (2015) 164-170. https://doi.org/10.1016/j.jnucmat.2015.03.011.
[24] H. Shi, R. Fetzer, C.C. Tang, D.V. Szabó, S. Schlabach, A. Heinzel, A. Weisenburger, A. Jianu, G. Müller, The influence of Y and Nb addition on the corrosion resistance of Fe-Cr-Al-Ni model alloys exposed to oxygen-containing molten Pb, Corros. Sci. 179 (2020) 109152. https://doi.org/10.1016/j.corsci.2020.109152.

[25] J.W. Yeh, S.K. Chen, S.J. Lin, J.Y. Gan, T.S. Chin, T.T. Shun, C.H. Tsau, S.Y. Chang, Nanostructured high-entropy alloys with multiple principal elements: novel alloy design concepts and outcomes, Adv. Eng. Mater. 6 (2004) 299-303. https://doi.org/10.1002/adem.200300567.
[26] B. Cantor, I.T.H. Chang, P. Knight, A.J.B. Vincent, Microstructural development in equiatomic multicomponent alloys, Mater. Sci. Eng. A 375 (2004) 213-218. https://doi.org/10.1016/j.msea.2003.10.257.
[27] Z. Li, K.G. Pradeep, Y. Deng, D. Raabe, C.C. Tasan, Metastable high-entropy dual-phase alloys overcome the strength–ductility trade-off, Nature 534 (2016) 227-230. https://doi.org/10.1038/nature17981.
[28] D.B. Miracle, O.N. Senkov, A critical review of high entropy alloys and related concepts, Acta Mater. 122 (2017) 448-511. https://doi.org/10.1016/j.actamat.2016.08.081.
[29] E.P. George, W.A. Curtin, C.C. Tasan, High entropy alloys: A focused review of mechanical properties and deformation mechanisms, Acta Mater. 188 (2020) 435-474. https://doi.org/10.1016/j.actamat.2019.12.015.
[30] J.W. Yeh, Y.L. Chen, S.J. Lin, S.K. Chen, High-entropy alloys–a new era of exploitation, Mater. Sci. Forum 560 (2007) 1-9. https://doi.org/10.4028/www.scientific.net/MSF.560.1.
[31] Y. Zhang, T.T. Zuo, Z. Tang, M.C. Gao, K.A. Dahmen, P.K. Liaw, Z.P. Lu, Microstructures and properties of high-entropy alloys, Prog. Mater. Sci. 61 (2014) 1-93. https://doi.org/10.1016/j.pmatsci.2013.10.001.
[32] Y. Zhang, Y.J. Zhou, J.P. Lin, G.L. Chen, P.K. Liaw, Solid-solution phase formation rules for multi-component alloys, Adv. Eng. Mater. 10 (2008) 534-538. https://doi.org/10.1002/adem.200700240.
[33] X. Yang, Y. Zhang, Prediction of high-entropy stabilized solid-solution in multi-component alloys, Mater. Chem. Phys. 132 (2012) 233-238. https://doi.org/10.1016/j.matchemphys.2011.11.021.
[34] S. Guo, C. Ng, J. Lu, C.T. Liu, Effect of valence electron concentration on stability of fcc or bcc phase in high entropy alloys, J. Appl. Phys. 109 (2011) 103505. https://doi.org/10.1063/1.3587228.
[35] Z. Wang, S. Guo, C.T. Liu, Phase selection in high-entropy alloys: from nonequilibrium to equilibrium, Jom 66 (2014) 1966-1972. https://doi.org/10.1007/s11837-014-0953-8.
[36] T.M. Butler, M.L. Weaver, Oxidation behaviour of arc melted AlCoCrFeNi multi-component high-entropy alloys, J. Alloys Compd. 674 (2016) 229-244. https://doi.org/10.1016/j.jallcom.2016.02.257.
[37] J. Lu, Y. Chen, H. Zhang, L. Li, L. Fu, X. Zhao, F.W. Guo, P. Xiao, Effect of Al content on the oxidation behaviour of Y/Hf-doped AlCoCrFeNi high-entropy alloy, Corros. Sci. (2020) 108691. https://doi.org/10.1016/j.corsci.2020.108691.
[38] J. Zhu, S. Lu, Y. Jin, L. Xu, X. Xu, C. Yin, Y. Jia, High-Temperature Oxidation Behaviours of AlCoCrFeNi High-Entropy Alloy at 1073–1273 K, Oxid. Met. 94 (2020) 265-281. https://doi.org/10.1007/s11085-020-09991-6.
[39] H. Ocken, Reducing the cobalt inventory in light water reactors, Nucl. Technol. 68 (1985) 18-28. https://doi.org/10.13182/NT85-A33563.
[40] T. Sakuma, Y.I. Yoshizawa, H. Suto, The microstructure and mechanical properties of yttria-stabilized zirconia prepared by arc-melting, J. Mater. Sci. 20 (1985) 2399-2407. https://doi.org/10.1007/BF00556069.
[41] J. Joseph, T. Jarvis, X. Wu, N. Stanford, P. Hodgson, D.M. Fabijanic, Comparative study of the microstructures and mechanical properties of direct laser fabricated and arc-melted AlxCoCrFeNi high entropy alloys, Mater. Sci. Eng. A 633 (2015) 184-193. https://doi.org/10.1016/j.msea.2015.02.072.
[42] C. Fazio, I. Ricapito, G. Scaddozo, G. Benamati, Corrosion behaviour of steels and refractory metals and tensile features of steels exposed to flowing PbBi in the LECOR loop, J. Nucl. Mater. 318 (2003) 325-332. https://doi.org/10.1016/S0022-3115(03)00009-6.
[43] A. Ul-Hamid, A Beginners' Guide to Scanning Electron Microscopy, Springer, Cham, 2018.

[44] L.J. Santodonato, Y. Zhang, M. Feygenson, C.M. Parish, M.C. Gao, R.J. Weber, J.C. Neuefeind, Z. Tang, P.K. Liaw, Deviation from high-entropy configurations in the atomic distributions of a multi-principal-element alloy, Nat. Commun. 6 (2015) 1-13. https://doi.org/10.1038/ncomms6964.
[45] J.C. Rao, H.Y. Diao, V. Ocelík, D. Vainchtein, C. Zhang, C. Kuo, Z. Tang, W. Guo, J.D. Poplawsky, Y. Zhou, P.K. Liaw, J.Th.M.De Hosson, Secondary phases in AlxCoCrFeNi high-entropy alloys: An in-situ TEM heating study and thermodynamic appraisal, Acta Mater. 131 (2017) 206-220. https://doi.org/10.1016/j.actamat.2017.03.066.
[46] A. Weisenburger, A. Jianu, W. An, R. Fetzer, M. Del Giacco, A. Heinzel, G. Müller, V.G. Markov, A.D. Kasthanov, Creep, creep-rupture tests of Al-surface-alloyed T91 steel in liquid lead bismuth at 500 and 550 ˚C, J. Nucl. Mater. 431 (2012). 77-84. https://doi.org/10.1016/j.jnucmat.2011.11.027.
[47] X.X. Yu, M.A. Taylor, J.H. Perepezko, L.D. Marks, Competition between thermodynamics, kinetics and growth mode in the early-stage oxidation of an equimolar CoCrFeNi alloy, Acta Mater. 196 (2020) 651-659. https://doi.org/10.1016/j.actamat.2020.06.056.
[48] H.E. Kadiri, R. Molins, Y. Bienvenu, M.F. Horstemeyer, Abnormal high growth rates of metastable aluminas on FeCrAl alloys, Oxid. Met. 64 (2005) 63-97. https://doi.org/10.1007/s11085-005-5715-0.
[49] S. Praveen, H.S. Kim, High-Entropy Alloys: Potential Candidates for High-Temperature Applications–An Overview, Adv. Eng. Mater. 20 (2018) 1700645. https://doi.org/10.1002/adem.201700645.
[50] S. Thangaraju, E. Bouzy, A. Hazotte, Phase stability of a mechanically alloyed CoCrCuFeNi high entropy alloy, Adv. Eng. Mater. 19 (2017) 1700095. https://doi.org/10.1002/adem.201700095
[51] W.R. Wang, W.L. Wang, J.W. Yeh, Phases, microstructure and mechanical properties of AlxCoCrFeNi high-entropy alloys at elevated temperatures, J. Alloys Compd. 589 (2014) 143-152. https://doi.org/10.1016/j.jallcom.2013.11.084.
[52] T.M. Butler, M.L. Weaver, Investigation of the phase stabilities in AlNiCoCrFe high entropy alloys, J. Alloys Compd. 691 (2017) 119-129. https://doi.org/10.1016/j.jallcom.2016.08.121.
[53] C. Ng, S. Guo, J. Luan, S. Shi, C.T. Liu, Entropy-driven phase stability and slow diffusion kinetics in an $Al_{0.5}$CoCrCuFeNi high entropy alloy, Intermetallics 31 (2012) 165-172. https://doi.org/10.1016/j.intermet.2012.07.001.
[54] F. Otto, A. Dlouhý, K.G. Pradeep, M. Kuběnová, D. Raabe, G. Eggeler, E.P. George, Decomposition of the single-phase high-entropy alloy CrMnFeCoNi after prolonged anneals at intermediate temperatures, Acta Mater. 112 (2016) 40-52. https://doi.org/10.1016/j.actamat.2016.04.005.
[55] C.C. Hsieh, W. Wu, Overview of intermetallic sigma (σ) phase precipitation in stainless steels, Isrn Metallurgy, 2012. https://doi.org/10.5402/2012/732471.
[56] G. Laplanche, S. Berglund, C. Reinhart, A. Kostka, F. Fox, E.P. George, Phase stability and kinetics of σ-phase precipitation in CrMnFeCoNi high-entropy alloys, Acta Mater. 161 (2018) 338-351. https://doi.org/10.1016/j.actamat.2018.09.040.
[57] T.T. Shun, Y.C. Du, Microstructure and tensile behaviours of FCC $Al_{0.3}$CoCrFeNi high entropy alloy, J. Alloys Compd. 479 (2009) 157-160. https://doi.org/10.1016/j.jallcom.2008.12.088.
[58] R. Wang, K. Zhang, C. Davies, X. Wu, Evolution of microstructure, mechanical and corrosion properties of AlCoCrFeNi high-entropy alloy prepared by direct laser fabrication, J. Alloys Compd. 694 (2017) 971-981. https://doi.org/10.1016/j.jallcom.2016.10.138.
[59] B. Gwalani, V. Soni, M. Lee, S.A. Mantri, Y. Ren, R. Banerjee, Optimizing the coupled effects of Hall-Petch and precipitation strengthening in a $Al_{0.3}$CoCrFeNi high entropy alloy, Mater. Des. 121 (2017) 254-260. https://doi.org/10.1016/j.matdes.2017.02.072.
[60] Y. Yamamoto, M.P. Brady, M.L. Santella, H. Bei, P.J. Maziasz, B.A. Pint, Overview of strategies for high-temperature creep and oxidation resistance of alumina-forming austenitic stainless steels, Metall. Mater. Trans. A 42 (2011) 922-931. https://doi.org/10.1007/s11661-010-0295-2.

[61] A. Takeuchi, A. Inoue, Classification of bulk metallic glasses by atomic size difference, heat of mixing and period of constituent elements and its application to characterization of the main alloying element, Mater. Trans 46 (2005) 2817-2829. https://doi.org/10.2320/matertrans.46.2817.
[62] M.A.E. Jepson, R.L. Higginson, In situ observation of the oxidation of S32101 duplex stainless steel at 900 °C, Corros. Sci. 59 (2012) 263-269. https://doi.org/10.1016/j.corsci.2012.03.011.
[63] Z. Tőkei, K. Hennesen, H. Viefhaus, H.J. Grabke, Diffusion of chromium in ferritic and austenitic 9–20 wt-% chromium steels, Mater. Sci. 16 (2000) 1129-1138. https://doi.org/10.1179/026708300101507055.
[64] Y.X. Liu, C.Q. Cheng, J.L. Shang, R. Wang, L.I. Peng, J. Zhao, Oxidation behaviour of high-entropy alloys AlxCoCrFeNi (x= 0.15, 0.4) in supercritical water and comparison with HR3C steel, Trans. Nonferrous Met. Soc. 25 (2015) 1341-1351. https://doi.org/10.1016/S1003-6326(15)63733-5.
[65] L. Chen, Z. Zhou, Z. Tan, D. He, K. Bobzin, L. Zhao, M. Öte, T. Königstein, High temperature oxidation behaviour of $Al_{0.6}CrFeCoNi$ and $Al_{0.6}CrFeCoNiSi_{0.3}$ high entropy alloys, J. Alloys Compd. 764 (2018) 845-852. https://doi.org/10.1016/j.jallcom.2018.06.036.
[66] C. Badini, F. Laurella, Oxidation of FeCrAl alloy: influence of temperature and atmosphere on scale growth rate and mechanism, Surf. Coat. Technol. 135 (2001) 291-298. https://doi.org/10.1016/S0257-8972(00)00989-0.
[67] S. Chevalier, Diffusion of oxygen in thermally grown oxide scales, Defect Diffus. Forum 289 (2009) 405-412. https://doi.org/10.4028/www.scientific.net/DDF.289-292.405.
[68] F.A. Golightly, G.C. Wood, F.H. Stott, The early stages of development of α-Al_2O_3 scales on Fe-Cr-Al and Fe-Cr-Al-Y Alloys at high temperature, Oxid. Met. 14 (1980) 217-234. https://doi.org/10.1007/BF00604565.
[69] H. Cheng, H.S. Caram, W.E. Schiesser, J.M. Rickman, H.M. Chan, M.P. Harmer, Oxygen grain-boundary transport in polycrystalline alumina using wedge-geometry bilayer samples: Effect of Y-doping, Acta Mater. 58 (2010) 2442-2451. https://doi.org/10.1016/j.actamat.2009.12.030.
[70] K. Messaoudi, A.M. Huntz, B. Lesage, Diffusion and growth mechanism of Al_2O_3 scales on ferritic Fe-Cr-Al alloys, Mater. Sci. Eng.A 247 (1998) 248-262. https://doi.org/10.1016/S0921-5093(97)00711-9.
[71] T. Ogawa, A. Kuwabara, C.A. Fisher, H. Moriwake, K. Matsunaga, K. Tsuruta, S. Kitaoka, A density functional study of vacancy formation in grain boundaries of undoped α-alumina, Acta Mater. 69 (2014) 365-371. https://doi.org/10.1016/j.actamat.2014.01.059.
[72] S. Kitaoka, T. Matsudaira, M. Wada, Mass-transfer mechanism of alumina ceramics under oxygen potential gradients at high temperatures, Mater. Trans. 50 (2009) 1023-1031. https://doi.org/10.2320/matertrans.MC200803.
[73] A.H. Heuer, Oxygen and aluminum diffusion in α-Al_2O_3: how much do we really understand? J. Eur. Ceram. Soc. 28 (2008) 1495-1507. https://doi.org/10.1016/j.jeurceramsoc.2007.12.020.
[74] A.H. Heuer, D.B. Hovis, J.L. Smialek, B. Gleeson, Alumina scale formation: a new perspective, J. Eur. Ceram. Soc. 94 (2011) s146-s153. https://doi.org/10.1111/j.1551-2916.2011.04573.x.
[75] M. Le Gall, A.M. Huntz, B. Lesage, C. Monty, J. Bernardini, Self-diffusion in α-Al_2O_3 and growth rate of alumina scales formed by oxidation: effect of Y_2O_3 doping, J. Mater. Sci. 30 (1995) 201-211. https://doi.org/10.1007/BF00352151.
[76] S. Swaminathan, C. Mallika, N.G. Krishna, C. Thinaharan, T. Jayakumar, U.K. Mudali, Evolution of surface chemistry and morphology of oxide scale formed during initial stage oxidation of modified 9Cr–1Mo steel, Corros. Sci. 79 (2014) 59-68. https://doi.org/10.1016/j.corsci.2013.10.026.
[77] F.H. Stott, G.C. Wood, J. Stringer, The influence of alloying elements on the development and maintenance of protective scales, Oxid. Met. 44 (1995) 113-145. https://doi.org/10.1007/BF01046725.
[78] Z.G. Zhang, X.L. Zhang, L. Sheng, X. Teng, The effect of the third element Cr on oxidation behaviour of Fe-xCr-10Al (at.%) alloys at 900 ˚C, Corrosion 2 (2009). DOI: 10.2174/1876503300902010037.

[79] S.J. Rothman, L.J. Nowicki, G.E. Murch, Self-diffusion in austenitic Fe-Cr-Ni alloys, J. Phys. F: Met. Phys. 10 (1980) 383.
[80] F. Noli, P. Misaelides, K. Bethge, Aluminum diffusion in Al-implanted AISI 321 stainless steel using accelerator-based characterization techniques, Nuclear Instruments and Methods in Physics Research Section B: Beam Interactions with Materials and Atoms, 139 (1998) 322-326. https://doi.org/10.1016/S0168-583X(97)01010-0.
[81] N. Birks, G.H. Meier, F.S. Pettit, Introduction to the high temperature oxidation of metals, Cambridge University Press, Cambridge, New York, 2006.
[82] H. Shi, C. Tang, A. Jianu, R. Fetzer, A. Weisenburger, M. Steinbrueck, M. Grosse, R. Stieglitz, G. Müller, Oxidation behaviour and microstructure evolution of alumina-forming austenitic & high entropy alloys in steam environment at 1200° C, Corros. Sci. 170 (2020) 108654. https://doi.org/10.1016/j.corsci.2020.108654.
[83] W.H. Tian, C.S. Han, M. Nemoto, Precipitation of α-Cr in B2-ordered NiAl, Intermetallics 7 (1999) 59-67. https://doi.org/10.1016/S0966-9795(98)00015-6.
[84] N.G. Jones, A. Frezza, H.J. Stone, Phase equilibria of an $Al_{0.5}$CrFeCoNiCu high entropy alloy, Mater. Sci. Eng. A 615 (2014) 214-221. https://doi.org/10.1016/j.msea.2014.07.059.
[85] W.H. Liu, T. Yang, C.T. Liu, Precipitation hardening in CoCrFeNi-based high entropy alloys, Mater. Chem. Phys. 210 (2018) 2-11. https://doi.org/10.1016/j.matchemphys.2017.07.037.
[86] N.T.C. Nguyen, P. Asghari-Rad, P. Sathiyamoorthi, A. Zargaran, C.S. Lee, H.S. Kim, Ultrahigh high-strain-rate superplasticity in a nanostructured high-entropy alloy, Nat. Commun. 11 (2020) 1-7. https://doi.org/10.1038/s41467-020-16601-1.
[87] B. Gwalani, S. Gorsse, D. Choudhuri, Y. Zheng, R.S. Mishra, R. Banerjee, Tensile yield strength of a single bulk $Al_{0.3}$CoCrFeNi high entropy alloy can be tuned from 160 MPa to 1800 MPa, Scr. Mater. 162 (2019) 18-23. https://doi.org/10.1016/j.scriptamat.2018.10.023.
[88] D. Choudhuri, B. Gwalani, S. Gorsse, M. Komarasamy, S.A. Mantri, S.G. Srinivasan, R.S. Mishra, R. Banerjee, Enhancing strength and strain hardenability via deformation twinning in fcc-based high entropy alloys reinforced with intermetallic compounds, Acta Mater. 165 (2019 420-430. https://doi.org/10.1016/j.actamat.2018.12.010.